Showcasing work from research groups of Professors Emilie Sauret and Yi-Chin Toh, School of Mechanical, Medical and Process Engineering, Queensland University of Technology (QUT), Australia. Artist: Louis Ong.

PoroFluidics: deterministic fluid control in porous microfluidics

This study presents a design framework for microfluidic devices with porous architectures, termed "poroFluidics", for controlling multi-phase fluid transport processes. By analyzing gas-liquid-solid interfaces and incorporating key properties of fluids and solids, the researchers demonstrate how to achieve consistent and desired flow patterns in porous media. The framework allows for precise control of spatial and temporal fluid invasion sequences through manipulation of solid geometry, flow conditions, and fluid/solid properties. This approach enables the development of multifunctional and dynamic porous media with potential applications in various fields. Copyright holder: Zhongzheng Wang

ROYAL SOCIETY
OF **CHEMISTRY**

rsc.li/loc

PoroFluidics: deterministic fluid control in porous microfluidics†

Zhongzheng Wang, [iD] ‡[a] Louis Jun Ye Ong,‡[abc] Yixiang Gan, [iD] [ef] Jean-Michel Pereira, [iD] [g] Jun Zhang, [iD] [h] Surasak Kasetsirikul,[ab] Yi-Chin Toh [iD] *[abcd] and Emilie Sauret [iD] *[a]

Microfluidic devices with open lattice structures, equivalent to a type of porous media, allow for the manipulation of fluid transport processes while having distinct structural, mechanical, and thermal properties. However, a fundamental understanding of the design principles for the solid structure in order to achieve consistent and desired flow patterns remains a challenge, preventing its further development and wider applications. Here, through quantitative and mechanistic analyses of the behavior of multi-phase phenomena that involve gas–liquid–solid interfaces, we present a design framework for microfluidic devices containing porous architectures (referred to as poroFluidics) for deterministic control of multi-phase fluid transport processes. We show that the essential properties of the fluids and solid, including viscosity, interfacial tension, wettability, as well as solid manufacture resolution, can be incorporated into the design to achieve consistent flow in porous media, where the desired spatial and temporal fluid invasion sequence can be realized. Experiments and numerical simulations reveal that different preferential flow pathways can be controlled by solid geometry, flow conditions, or fluid/solid properties. Our design framework enables precise, multifunctional, and dynamic control of multi-phase transport within engineered porous media.

Introduction

The development in the manipulation of fluids in open microfluidic devices has enabled numerous applications in materials science, biotechnology, and healthcare.[1,2] An emerging area of research in this field is the control of fluid transport processes in materials with microscale lattice structures, which can be fabricated by additive manufacturing methods. Unlike traditional enclosed microfluidic devices, this type of open porous material allows for fluid flow control while offering the ability to adjust its mechanical, thermal, and structural properties.[3–8] Owing to its porous structure, multiple streams of fluids can be simultaneously achieved in a single volume, demonstrating excellent potential for the parallelization of multiple fluid channels and high interfacial areas that facilitate mixing/reaction processes.[9] Although efforts have been made to advance the fundamental understanding of the fluid transport processes in the micro-architected materials with lattice structures,[4,10–12] most investigations have focused on single-phase flow. A recent notable work by Dudukovic *et al.*[9] demonstrated the precise manipulation of multi-phase flow in the open lattice structures, where capillary-driven fluid flow along preferential pathways is achieved. This led to the realization of various applications, such as selective metallization of pre-programmed patterns and control of mixing and diffusion of different fluids.

While numerous potential applications have been identified, the lack of fundamental understanding regarding the design principles for creating generalized open lattice structures to control fluid flow remains a challenge, hindering their broader adoption. Therefore, there is a pressing need for quantitative and mechanistic analysis to understand the fluid–solid interaction within open porous microfluidic systems.

Multi-phase flow in porous media has been a classical area of research in the context of geological systems, *i.e.*, soils

[a] School of Mechanical, Medical and Process Engineering, Faculty of Engineering, Queensland University of Technology, QLD 4001, Australia.
E-mail: yichin.toh@qut.edu.au, emilie.sauret@qut.edu.au
[b] Centre for Biomedical Technologies, Queensland University of Technology, QLD 4059, Australia
[c] Max Planck Queensland Centre, Queensland University of Technology, QLD 4059, Australia
[d] Centre for Microbiome Research, Queensland University of Technology, QLD 4102, Australia
[e] School of Civil Engineering, The University of Sydney, NSW 2006, Australia
[f] Sydney Nano, The University of Sydney, NSW 2006, Australia
[g] Navier, Ecole des Ponts, Univ Gustave Eiffel, CNRS, Marne-la-Vallée, France
[h] Queensland Micro and Nanotechnology Centre, Griffith University, Brisbane, QLD 4111, Australia
† Electronic supplementary information (ESI) available. See DOI: https://doi.org/10.1039/d4lc00518j
‡ These authors contributed equally to this work.

and rocks, with applications in water infiltration, enhanced oil recovery and CO_2 geosequestration.[13–17] Extensive efforts have been devoted to understanding and predicting the fluid transport processes *via* experimental, numerical, and theoretical approaches.[18–24] It is well established that the pattern in which one fluid displaces another can be either stable, with a uniform and compact invasion, or unstable, showing branching, finger-like shapes. This pattern depends on both the characteristics of the fluids and the conditions under which they flow.[18] At the same time, wettability, *i.e.*, the fluids' affinity to the solid structure, has also shown to have a significant impact on multi-phase flows.[25–27] Apart from focusing on the effects of fluid phases, several recent investigations have examined the role of structural and geometrical features of porous structures on multi-phase flow.[22,28–32] It is found that a more disordered porous structure, generally characterized by greater spatial fluctuations in porosity, promotes the transition from stable displacement to the unstable fingering regime.[28,29] However, most existing studies focus on developing more accurate analytical models to predict average flow behavior in porous media. The knowledge gained has not yet been fully utilized to design devices containing porous architectures that allow for precise control of fluid transport processes.

Here, we present a framework for designing porous microfluidic devices, called poroFluidics, for deterministic control of the multi-phase flow transport process. Through quantitative analysis of the fundamental mechanisms of fluid invasion processes, particularly the solid–liquid–air interface motion at the pore scale, we numerically and experimentally show that the temporal and spatial control of flow in porous media can be achieved.

Results and Discussion

Fluid control mechanisms in poroFluidic devices

The porous microfluidics (poroFluidics) considered in this work are represented by fluid flow through a simple structural configuration, *i.e.*, parallel plates (Hele-Shaw cells) with cylindrical posts arranged in-between on a triangular lattice (Fig. 1). Despite its geometrical simplicity, this system contains the key feature of porous media with the presence of interconnected pore space associated with diverging and converging sections. The overall framework for designing poroFluidics to achieve precise control of multi-phase flow is shown in Fig. 1. The input parameters are the desired fluid pathways and fluid–solid interaction properties, which include the fluid–fluid interfacial tension, viscosity, wettability (quantified by contact angle θ measured within the invading fluid), and the geometrical resolution of the fabricated solid structure [Fig. 1(A)]. By controlling the location and size of the cylindrical posts for given fluid
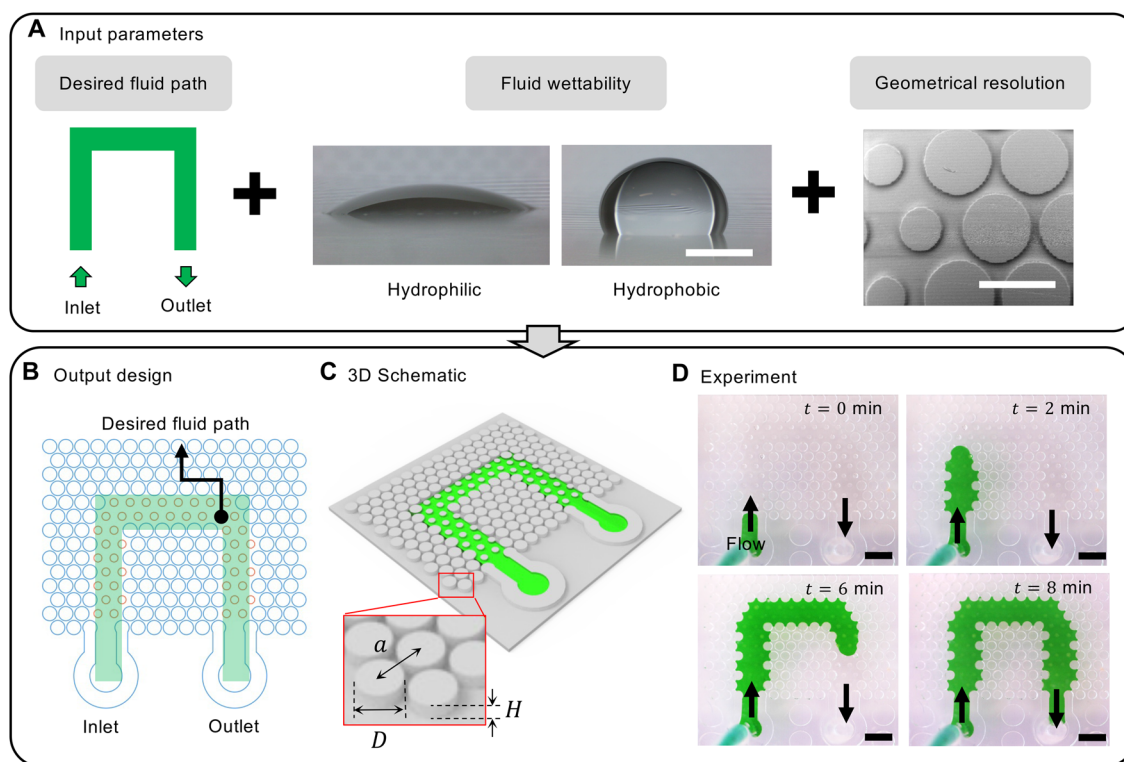
Fig. 1 Framework of designing poroFluidic devices for multi-phase flow control. (A) Inputs for poroFluidic design include desired fluid path, fluid wettability, and achievable geometrical resolution. (B) Schematic showing the designed poroFluidic composed of cylindrical posts with a height H = 300 μm arranged on a triangular lattice with a center-to-center spacing a = 1 mm. Red and blue circles have diameters D = 500 μm and D = 887 μm, respectively. (C) 3D schematic showing the design. The top surface of the design is not shown. (D) Sequential snapshots during an injection experiment of green-dyed water. Arrows indicate flow direction. All scale bars equal 2 mm.

properties, the deterministic control of fluid invasion process in the poroFluidics can be achieved. Fig. 1(D) shows the sequential top-view snapshots during a green-dyed water injection experiment on a polydimethylsiloxane (PDMS)-based poroFluidic device, where the fluid invasion path follows the programmed inverted "U" shape.

### Mechanistic analysis for multi-phase flow processes

The behavior of multi-phase flow in a poroFluidic device can be governed by gravitational, inertial, viscous, and capillary effects. The corresponding dimensionless groups include Reynolds number (Re = $\rho u D/\mu$), bond number (Bo = $\rho g D^2/\gamma$), and capillary number (Ca = $\mu u/\gamma$), with ρ density, u velocity, D characteristic length, μ dynamic viscosity, and γ interfacial tension. Since the characteristic length D is typically at millimeters to micrometers and the flow velocity is usually small (much less than 1 m s^{-1}) for microfluidic applications,

these dimensionless numbers are usually much smaller than one at the pore scale, indicating that the flow condition falls within the capillary-dominated flow regimes where the effects of gravity, inertia, and viscosity are insignificant compared to capillary forces.

To quantify the flow resistance due to the capillary effect as the meniscus travels between a pair of posts [Fig. 2(A) inset, meniscus moves from left to right associated with increasing α], the Laplace pressure can be calculated by $P_c = \gamma(1/R_{in} + 1/R_{out})$, where the out-of-plane radius of curvature $R_{out} = h/(2\gamma \cos\theta)$, and h is the height of the microfluidic channel. The in-plane radius of curvature R_{in} can be calculated as:[33]

$$R_{in} = \frac{r\cos\alpha - a/2}{\cos(\alpha + \theta)}, \tag{1}$$

where a is the center-to-center spacing of posts and α is the angle associated with the meniscus position. Since we consider a planar structure with no variation in the height h
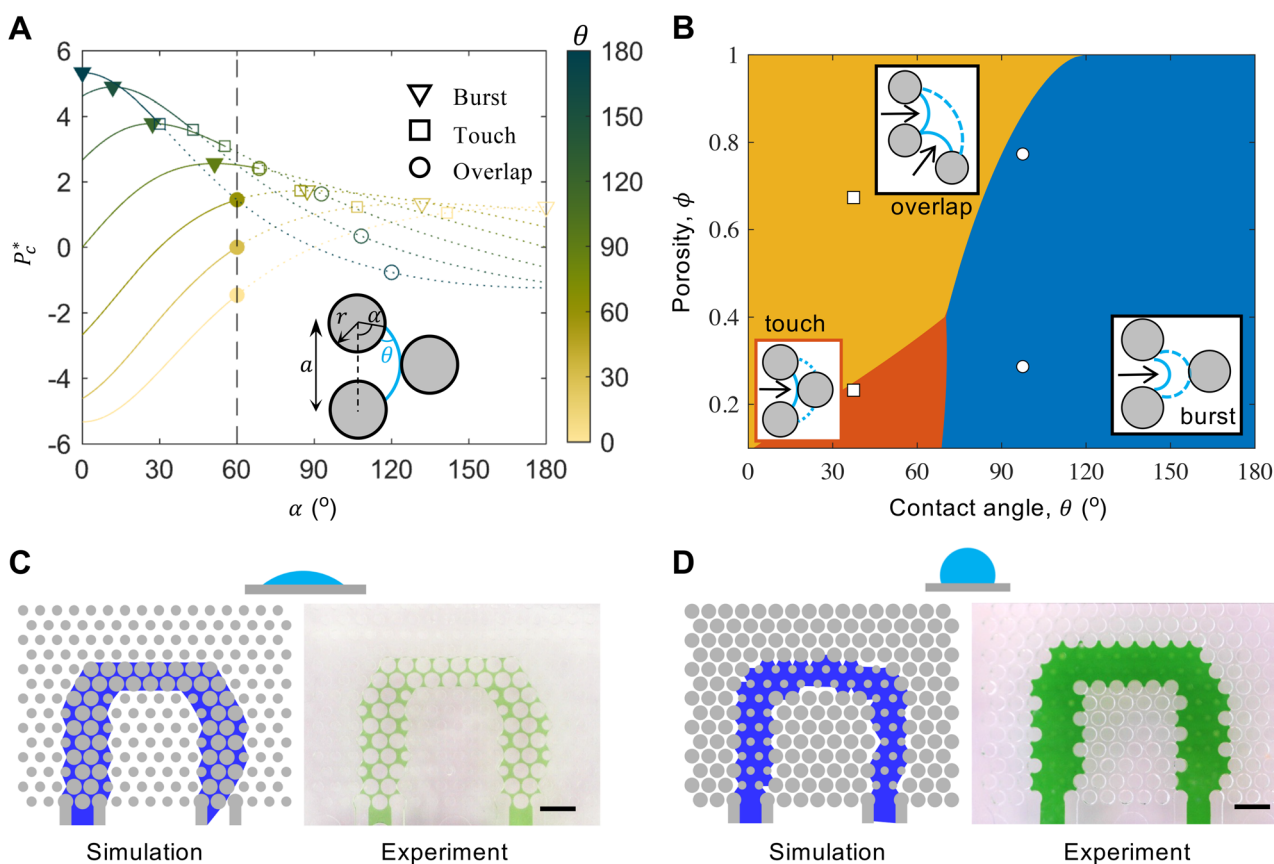
Fig. 2 Analysis of pore-scale mechanisms enables fluid control under different wettability conditions. (A) The dimensionless capillary pressure P_c^* as a meniscus between two posts advances under different contact angles. The location of the meniscus is represented by α in the inset. This plot corresponds to a porous medium with a porosity $\phi = 0.65$. The burst, touch, and overlap events are marked by triangles, squares, and circles, respectively. The first instability event a meniscus encounters is denoted by filled markers. P_c^* after touch or overlap events are represented by dashed lines (analytical but not realistic values that a meniscus cannot experience due to the occurrence of merging/splitting events). The black-dashed line marks the characteristic angle for overlap, which is 60° for circles placed on a triangular lattice. (B) Critical event phase diagram in the ϕ–θ space. The porosity ϕ is calculated based on a repeating unit cell with cylindrical posts placed on a triangular lattice $\phi = 1 - (2\sqrt{3}\pi r^2)/(3a^2)$, where $a = 1$ mm is the post center-to-center spacing. Insets show the schematics of burst, touch, and overlap events. (C) Numerical (left) and experimental (right) results on the flow path with $\theta = 37.4°$ and posts diameters 600 μm and 914 μm [conditions indicated by square markers in (B), respectively]. The injection rate is 0.16 μL min^{-1}. (D) Simulation and experiment with $\theta = 100.4°$ and posts diameters 500 μm and 887 μm [circular markers in (B)]. The injection rate is 2 μL min^{-1}. All scale bars correspond to 2 mm.

of the microfluidic device, the out-of-plane component remains constant for a given solid structure and fluid property. Therefore, to highlight the differences in capillary resistances among menisci, which directly govern the sequence of fluid advancement, we define and plot the dimensionless capillary pressure $P_c^* = a/R_{in}$ in Fig. 2(A) for different contact angles θ. As the meniscus advances, it may experience pore-scale instabilities including burst, touch, or overlap[34] [corresponding schematics shown in the insets Fig. 2(B)]. During the movement of the meniscus, the burst event corresponds to the meniscus configuration when P_c^* reaches its maximum value, where α satisfies:

$$\sin(\alpha + \theta)\left(\frac{a}{2r} - \cos\alpha\right) + \sin\alpha\cos(\alpha + \theta) = 0. \quad (2)$$

The touch event occurs when the meniscus comes into contact with the post at the front, which geometrically satisfies:

$$\left[1 - \cos\left(\alpha + \theta - \frac{\pi}{2}\right)\right]R_{in} + r\sin\alpha = \frac{\sqrt{3}}{2}a - r. \quad (3)$$

Finally, the overlap event or the non-local cooperative pore filling[35] occurs when two menisci touch each other and merge:

$$\alpha_{overlap} = \max[\theta_c, 2\theta_c - \min(\alpha_{burst}, \alpha_{touch})], \quad (4)$$

where $\alpha_{overlap}$, α_{burst}, and α_{touch} are the α values at which overlap, burst, and touch events take place, respectively. θ_c is the characteristic angle of the porous media. For instance, for a triangular lattice, $\theta_c = 60°$.[35,36] These pore-scale invasion mechanisms have been shown to have significant impacts on the macroscopic invasion morphology for multi-phase flow, which can be quantified by the saturation or fractal dimension of the fluids that have invaded the porous medium.[24,37] Previous studies have indicated that multi-phase flow processes dominated by overlap events are associated with uniform and compact expansion of the invading fluid.[28,32,38] As a result, in order to achieve programmed fluid flow that follows specific geometrical pathways in structured porous media, the burst and touch instability mechanisms need to be exploited.

These three types of instabilities are denoted by triangles, squares, or circles in Fig. 2(A) for the case of a porosity $\phi = 0.65$, with the first instability that a meniscus encounters, i.e., the critical mechanism, represented by filled markers. The corresponding phase diagram of the critical pore-scale mechanism for different contact angles θ and porosity ϕ is plotted in Fig. 2(B). According to Fig. 2(B), if the contact angle is small (i.e., the solid structure is hydrophilic in the case of water injection), the porosity should be relatively low (or higher solid density) in order to exploit the touch mechanism. This is the approach adopted by Dudukovic et al.[9] to direct selected fluid pathways where the fluid preferentially fills regions with higher relative density for their hydrophilic polymers. On the other hand, when the

solid is hydrophobic, the burst mechanism can be harnessed with a wide range of porosity.

Fig. 2(C) shows the multi-phase flow numerical simulation using the pore-resolved interface tracking algorithm[24] (left) and experiment (right) for a poroFluidic device with hydrophilic surface (Movies S1 and S2†). It can be seen that the fluid preferentially fills the region with large posts [post radius $r = 457$ μm, denoted by the square marker in Fig. 2(B)], whereas regions with smaller posts [post radius $r = 300$ μm, denoted by the circle marker in Fig. 2(B)] remain occupied by air. A similar case for a hydrophobic porous medium is shown in Fig. 2(D), where an inverted "U" pattern is filled by the dyed water according to both numerical and experimental results (Movies S3 and S4†). Here, the fluid flow is guided by the smaller posts ($r = 250$ μm), and the region with higher relative density with larger posts remains uninvaded due to greater capillary resistance. These findings show that poroFluidic devices can be designed to effectively control fluid flow under various wetting conditions by exploiting different invasion mechanisms. We note that although the general fluid pathways between experiments and simulations in Fig. 2(C) and (D) are consistent, the menisci locations are not completely identical. This is because our critical capillary pressure analysis is performed assuming uniform pillar sizes, leading to a buffer zone in the regions of transition between large and small posts. Please refer to ESI† (ESI Text and Fig. S3) for more details on the evaluation of the fluid paths.

Additionally, we note that despite the phase diagram shown in Fig. 2(B) spans the whole range of contact angle, our analysis of the pore-scale invasion mechanisms is based on a pseudo-2D assumption and does not consider the corner flow phenomenon, which may appear at small contact angle under certain geometrical conditions.[37,39,40]

Incorporating variations to ensure the robustness of poroFluidic designs

Achieving consistent fluid patterning as shown in Fig. 2(C) and (D) can be difficult in practice due to several sources of uncertainty or variations in fluid properties. Firstly, the contribution from viscous pressure drop during fluid injection into the poroFluidic device needs to be small enough such that the flow invasion process can be regulated by capillary forces. This requires that the difference in the capillary pressures ΔP_c for menisci in regions between big and small posts is greater than the total viscous pressure drop ΔP_v, i.e., $\Delta P_c > \Delta P_v$ where

$$\Delta P_c = \gamma\left(\frac{1}{R_{in,1}} + \frac{1}{R_{out,1}}\right) - \gamma\left(\frac{1}{R_{in,2}} + \frac{1}{R_{out,2}}\right) = \gamma\left(\frac{1}{R_{in,1}} - \frac{1}{R_{in,2}}\right), \quad (5)$$

where $R_{in,1}$ and $R_{in,2}$ are the in-plane radii of curvature at critical mechanism (either burst or touch) for big and small posts, respectively, and $R_{out,1} = R_{out,2}$ are the out-of-plane curvatures, being the same as a result of uniform

wettability and channel height. ΔP_v is estimated by the Darcy–Weisbach equation:

$$\Delta P_v = \frac{128\mu QL}{\pi D_H^4},\qquad(6)$$

where L is the total length of the designed flow path, Q is the injection rate, and D_H is the hydraulic diameter defined as $D_H = 4A/P$ with A the cross-sectional area of the flow and P the wetted parameter. The geometrical parameters are calculated conservatively using the dimensions at the throats (narrowest region): $A = H(a - D)$ and $P = 2(H + a - D)$, where H is the pillar height, a is the pillar center-to-center spacing, and D is the pillar diameter. Eqn (6) thus gives the maximum viscous pressure drop when the invading fluid reaches the outlet. Therefore, the constraint $\Delta P_c > \Delta P_v$ implies that the injection rate should be slow enough such that the viscous pressure drop should not exceed the differential capillary pressures throughout the whole invasion process.

It is useful to estimate the time required to complete an injection process via a simple scaling analysis. In the case of periodic unit-based architectures, the total length of the flow path can be denoted by $L = Nl$, where l represents the typical size of a single unit (or one pore space), and N is the number of such units in the pre-defined pathways. This allows the determination of the characteristic injection rate $Q \sim \gamma l^2/\mu N$. With the total volume of the fluid path to be filled $V \sim Nl^3$, the time needed to finish the fluid invasion, t, can be

estimated as $t \sim l\mu N^2/\gamma$. Essentially, this means that systems with larger final patterns or greater fluid viscosity will generally take longer to fill.

The design of poroFluidic devices should also take into account variations in surface properties, such as contact angles, and limitations in fabrication methods, like 3D printing resolution. This can be done by examining the critical capillary pressure P_{crit}^*, which is the P_c^* value at which interfacial instability occurs by either burst [eqn (2)], touch [eqn (3)] or overlap [eqn (4)] mechanisms. Fig. 3(A) maps out these critical pressures in the porosity vs. contact angle (ϕ–θ) space. The equal-critical pressure lines are shown as black-dashed lines. The colorbar transition from a linear to a logarithmic scale has been applied for better visualization.

To demonstrate how uncertainties arising from fabrication errors or surface heterogeneity can be accounted for in the design of poroFluidics-mediated flow, we choose a large post [marked by a blue circle Fig. 3(A)] as a reference. The potential variations in contact angles and post sizes are represented as the dimensions of a rectangle in Fig. 3(A). Specifically, the rectangle's width and height represent the range of variation for experimentally measured contact angles and post sizes respectively. The half-width of the rectangle represents two standard deviations of the measured contact angle, where the standard deviation was $\delta_\theta = 4.28°$; while the half-height represents the porosity variation calculated based on two standard deviations of the measured post size, where the standard deviation was $\delta_r = 5.67$ μm. This rectangle effectively
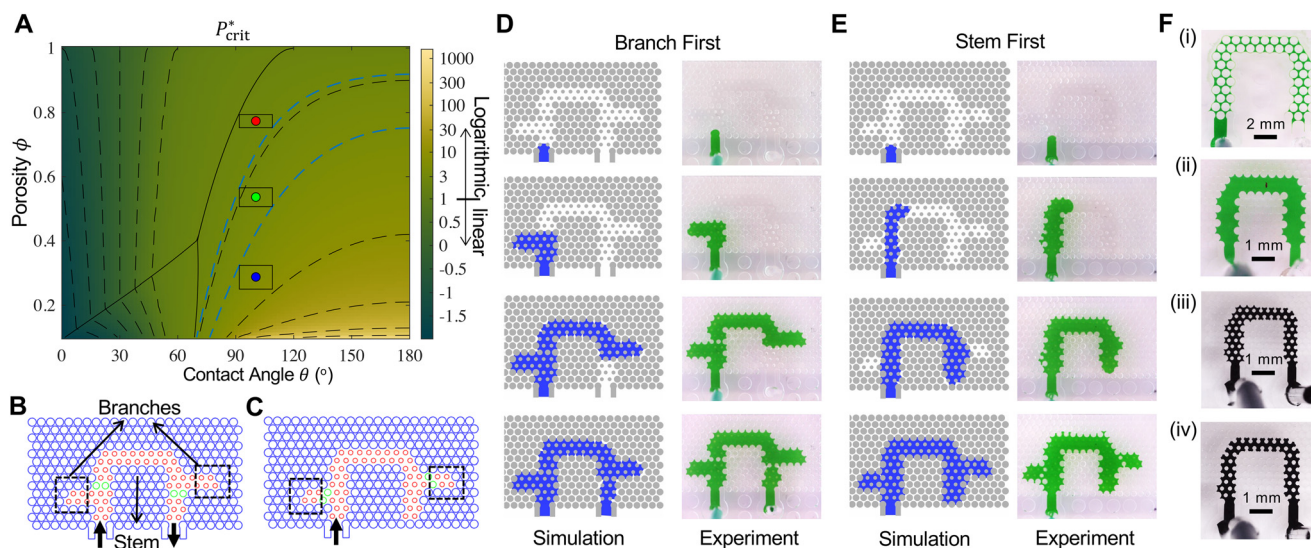
Fig. 3 Incorporating variations to ensure the robustness of poroFluidic designs. (A) Critical dimensionless capillary pressure phase diagram. Black-solid lines denote the boundaries of three types of instability events [see Fig. 2(B)]. The circular markers represent the porosity and contact angle in the system [color-consistent with (B) and (C)]. The width and height of rectangles, respectively, represent the uncertainties from contact angle and geometry. Dashed lines are equi-P_c^* lines. (B) Schematic showing the poroFluidic design for branch-first (enclosed by boxes) filling sequence and (C) stem-first filling sequence. Red, green, and blue posts have diameters of 500 μm, 715 μm, and 887 μm, respectively. (D) Snapshots of simulation (left) and experiment (right) for a branch-first invasion and (E) stem-first invasion. Average contact angle $\theta = 100.4°$. (F) Final fluid (green-dyed water) patterns with (i) absent surrounding pillars under the hydrophilic condition with $\theta = 37.4°$, and (ii) absent inner pillars under the hydrophobic condition with $\theta = 100.4°$. The conductive carbon paint–water mixtures (black) with volume ratios 1:10 (iii) and 1:1 (iv) are also used for forming the fluid pathways. The dynamic viscosities of the conductive liquids are 7.4 mPa s and 46.9 mPa s, being approximately 8 times and 50 times greater than water, respectively.

outlines the probable range for P^*_{crit}, where there is a 97.9% likelihood that the actual value falls within this area, assuming a normal distribution for the measured uncertainties. To exploit the burst mechanism, P^*_{crit} within the porous region filled with green posts must be smaller, *i.e.*, the rectangle cannot intersect with the minimum equi-P^*_{crit} line (dashed-blue curve) from the larger blue posts. This ensures that during the fluid injection process where the fluid invades pores with the least resistance, the targeted larger pores (associated with smaller posts) will be preferentially invaded even with the uncertainties in θ and ϕ. By doing so, we can better control fluid behavior even when accounting for uncertainties.

Following this criterion, one can achieve different fluid patterning pathways for given uncertainties in wettability and geometry resolution. Fig. 3(B) and (C) show schematics of poroFluidic designs containing three different sizes of posts, *i.e.*, 500 μm (red circles), 715 μm (green circles), and 887 μm (blue circles) [also Fig. 3(A)]. We note the difference between the heights of the rectangles with the same absolute uncertainty in post radius, r. This is due to the conversion from post radius r to porosity $\phi = 1 - (2\sqrt{3}\pi r^2)/(3a^2)$, where $a = 1$ mm is the post center-to-center spacing. Compared to red and blue posts, the green posts have an intermediate value of critical capillary pressure (P^*_{crit}), functioning as capillary barriers that dictate the flow sequence - whether it is the stem or the branches that get preferentially filled. Fig. 3(D) and (E) show the snapshots of two different fluid invasion paths: one filling the branch before the stem and the other filling the stem before the branch (ESI† Movies S5–S8).

We note that according to Fig. 3(A), if needed, the size of red pillars in Fig. 3(B and C) can be smaller as long as the corresponding P^*_{crit} is below the equi-P^*_{c} line. This means that the controlled sequential flow can still be achieved in the extreme case where the pillar size of red posts is zero, *i.e.*, in the case with the absence of the red pillars. Similarly, this means that if the smaller pillars in Fig. 2(C and D) are removed, the fluid pathways are expected to remain the same. As evidenced in Fig. 3(F-i and ii), fluid pathways in the shape of an inverted "U" can be formed for devices with the same geometry and wetting condition as in Fig. 2(C and D), but without the smaller surrounding or inner pillars.

Further, to thoroughly demonstrate the robustness of poroFluidic designs, it is worth examining the flow control capability with different fluids. Here, two solutions of conductive carbon paint–water mixtures with volume ratios of 1:10 and 1:1 are prepared, and the corresponding dynamic viscosities are measured to be 7.4 mPa s and 46.9 mPa s, being approximately 8 times and 50 times greater than water, respectively. The contact angles of these liquids on PDMS were measured to be 102.3° and 99.2°, respectively. Based on the new fluid properties, injection rates of 0.1 μL min^{-1} and 0.02 μL min^{-1} were imposed at the inlet. Fig. 3(F-iii) and (iv) show that the desired flow pathway can be achieved for fluids with viscosities much higher than water. We also want to highlight that the devices in Fig. 3(F-ii) to (iv) have a geometry with 1/2 size of the one

in Fig. 2(C). This is achieved *via* improving the manufacture resolution by using the standard SU-8 mold fabrication process.

Overall, our experimental and numerical results demonstrate that, by considering the capillary force, pressure drop due to fluid viscosity, and fabrication resolution into account, the poroFluidic framework enables not only the configuration of the final patterns of fluid distribution but also allows the precise control of the order in which the fluid invades different regions. This capability is especially crucial in applications like drug detection or sensors, where the sequence of multiple chemical reactions must be controlled. Moreover, the ability to precisely control various fluid types in poroFluidic devices could foster additional functions, such as in-built interdigitated circuits for sensing applications. As shown in Fig. 3(F), the conductive liquid can be manipulated to form an electrode within the poroFluidics device, which can be potentially applied for manufacturing integrated sensors without using laborious and time-consuming micro- or nanofabrication.

Multifunctionality with selective flow paths

In the poroFluidic devices reported here, the pore spaces are sub-millimeter in size, and smaller than the capillary length $l_{\text{cap}} = \sqrt{\gamma/\rho g}$, which is around 3 mm for a water–air interface. As a result, the effect of gravity is typically insignificant and has been disregarded. However, gravity can influence invasion paths when its force aligns with the flow direction. Fig. 4(A) illustrates a poroFluidic design with two programmed outlets, each activated depending on the orientation of the device and thus the role of gravity. When placed horizontally, making gravity negligible, fluids injected using the burst mechanism follow pathways with red pillars. This happens if their associated P^*_{crit} is smaller than those in the green and blue regions, directing the flow towards the "noG" outlet. Conversely, when the device is vertically oriented and gravity comes into play, the flow exits through the "wG" outlet under two conditions: (1) the difference in P^*_{crit} between the blue and red regions supports the liquid column rising to a height h_2; and (2) the P^*_{crit} difference between the red and green regions is less than h', triggering lateral flow due to gravitational pressure. Fig. 4(B) shows the P^*_{crit} map with red, green, and blue circles representing the posts' size and contact angles, *i.e.*, 500 μm, 589 μm, and 910 μm, respectively, with $\theta = 100.4°$. Fig. 4(C) and (D) respectively show the invasion sequences from the simulation without and with the effect of gravity, respectively, which is consistent with the expected outcome (ESI† Movies S9 and S10). We note that in this section, uncertainties in contact angle and geometry resolution were not considered since the critical pressure variation due to uncertainties from measured δ_θ and δ_r were greater than $\rho g h'$. Thus, fabrication methods with higher resolution than 3D printing and more consistent surface properties are needed to replicate these results experimentally.

The flow pathway can also be regulated when fluids have different wetting characteristics. Fig. 4(E) illustrates a design that bifurcates the flow either to the left or right based on
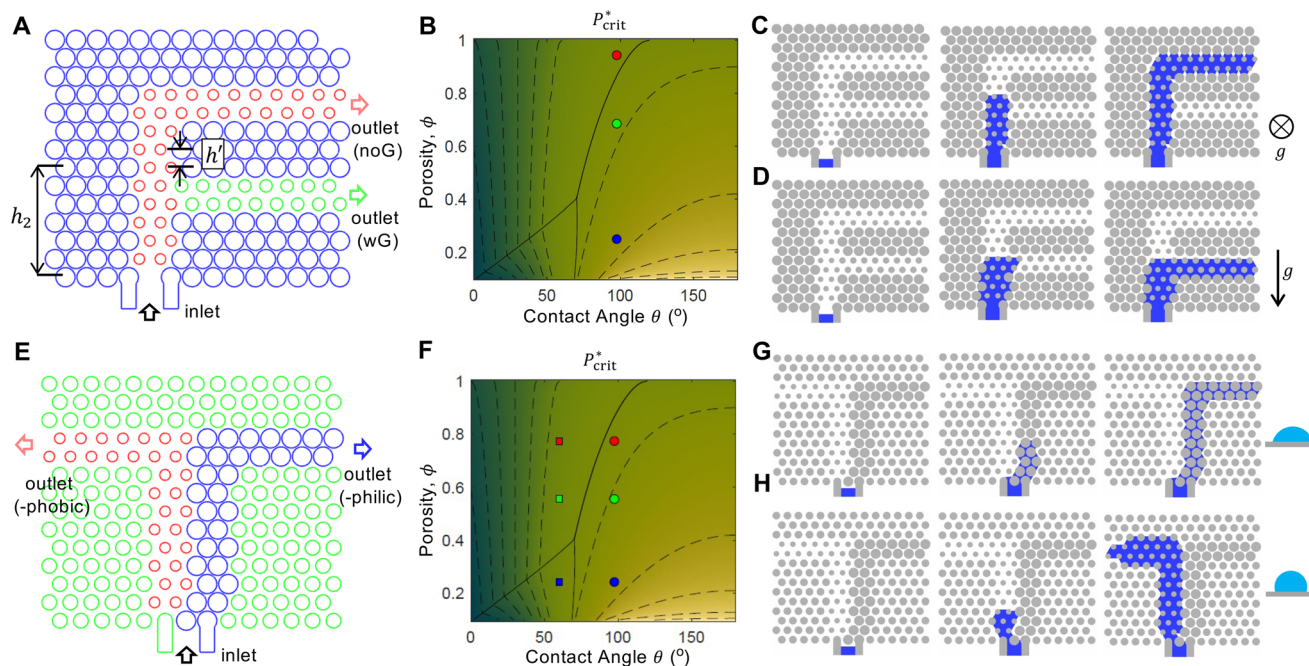
Fig. 4 Bifurcation of flow regulated by gravity and wettability. (A) Schematic showing the poroFluidic design with two targeted outlets depending on gravity. Red, green, and blue posts, respectively, have diameters of 500 μm, 589 μm, and 910 μm. (B) The corresponding ϕ–θ phase diagram with θ = 100.4° and different post sizes. (C) and (D) The simulation results on the invasion process without and with gravity. (E) PoroFluidic design with two targeted outlets depending on wettability. Red, green, and blue posts, respectively, have diameters of 500 μm, 700 μm, and 914 μm. (F) The corresponding ϕ–θ phase diagram. (G) and (H) The simulation results on the invasion processes with θ = 60°, and θ = 100.4°, respectively.

the contact angle. When the solid matrix is wetting to the invading fluid, the fluid tends to fill the more densely packed blue regions, governed by the touch mechanism. When the solid structure is non-wetting, the region with red (smallest) posts will be preferentially filled, where the burst mechanism is the critical one. Fig. 4(F) shows the corresponding critical pressure P^*_{crit} map with the markers highlighting various post sizes (diameters of 500 μm, 589 μm, and 910 μm) and contact angles (θ = 60°, and θ = 100.4°). The fluid invasion patterns from the numerical simulation in Fig. 4(G) and (H) confirmed the desired bifurcated flow pathways (ESI† Movies S11 and S12). These findings demonstrate the versatility of design space dimensions in controlling fluid flow, encompassing geometry, wettability, and gravitational effects.

Conclusion

We have proposed a framework for designing porous microfluidic devices, or poroFluidics, for spatial and temporal control of the multi-phase transport process. We quantitatively analyzed different types of pore-scale invasion mechanisms and provided insights into how interfacial instability events can inform the inverse design of pore structure to achieve programmed flow pathways. Importantly, these quantitative and mechanistic analyses not only enable accurate flow manipulation under different solid wetting conditions and fluid properties but also, for the first time, open the avenue to incorporate experimental uncertainties from manufacturing constraints and surface wetting heterogeneity into the design.

Consequently, it is demonstrated that poroFluidic devices with multiple hierarchies of critical capillary pressures allow the precise tuning of both the final fluid patterns and the sequences of invasion. We further showcased the feasibility of regulating flow paths with geometrically identical solid structures *via* gravity and wettability.

These results highlight the prospective applications in the fields of biomedical science, chemistry, pharmaceuticals, and materials science. The ability to accurately control the fluid pathways is valuable for achieving selective metallization of pre-programmed patterns in advanced manufacturing, and studying how drugs interact with different materials and surfaces in pharmaceutical research. The poroFluidic devices can also be leveraged in applications where the control over the fluid filling sequence (and consequently the chemical reactions) is essential, such as microscale diagnostics and chemical synthesis. Further, the demonstrated bifurcation of fluid flow could inspire the design of next-generation spontaneous immiscible fluid separation devices for separating and removing different phases, such as oil from water in the water purification process, or creating and controlling emulsions in the food industry. These applications demonstrate the versatility and potential impact of poroFluidic devices across various domains.

Although our work adopts a straightforward geometric framework - namely, planar configurations with circular posts arranged in a triangular lattice - the principles elucidated should be readily extensible to other lattice configurations[36] or more complex porous architectures through similar

mechanistic analyses and numerical simulations. Advancing our fundamental knowledge of the mechanisms governing pore-scale interfacial dynamics in micro-architected porous media remains crucial for achieving reliable flow control.

With the development of surface treatment techniques as well as better fabrication resolution of solid structures, we expect fluid patterns with much more complexity could be realized, which can facilitate broader applications of poroFluidics in materials science, biotechnology, and healthcare.

Materials and Methods

Device fabrication

The molds of the poroFluidic devices were designed with AutoCAD (ver 2020, AutoDesk, USA), which were subsequently 3D-printed using the ASIGA UV Max X27 (ASIGA, Australia), with PlasClear v2.0 resin (ASIGA, Australia). Layer thickness was kept constant at 50 μm. The exposure time for the resin was 13 seconds. The following procedure was followed to avoid the curing inhibition problem:[41] the 3D-printed mold was rinsed with isopropyl alcohol (IPA) before soaking in IPA for 2 hours to remove excess resin residues. After soaking, the mold was rinsed copiously with deionized water before air drying. The mold was then UV-cured for 30 minutes, after which it was baked in the oven at 70 °C for 48 hours. All molds were then subjected to silanization with trichloro(1*H*,1*H*,2*H*,2*H*-perfluorooctyl)silane in a vacuum for 2 hours before PDMS soft lithography. Unless otherwise stated, chemicals are procured from Sigma-Aldrich (Merck, Australia).

The poroFluidic devices were produced by replica molding polydimethylsiloxane (PDMS) on the 3D printed molds at a 10 : 1 elastomer to curing agent ratio (Slygard 184, Dow Corning, USA). The casted PDMS were heat cured at 70 °C for 4 hours before demolding. Inlets and outlets of the devices were created with a 1.5 mm OD biopsy punch (Robbins Instruments, USA). The demolded PDMS devices were treated with oxygen plasma onto a PDMS-coated coverslip made based on a previously established protocol.[42] Briefly, PDMS-coated coverslips were placed between a pair of polyurethane transparencies (SureMark, Singapore) separated by 340 μm glass spacers before being sandwiched between two aluminum plates. The sandwiched PDMS-coated coverslips were then cured at 70 °C for 4 hours. The PDMS-coated coverslips and the demolded PDMS devices were then treated in oxygen plasma with medium strength at 38 W for 60 seconds (PDC-002-HP Harrick Plasma Cleaner) before bonding.

Device characterisation

Transmission images of micro-posts within the PDMS poroFluidic devices were assessed using a Nikon ECLIPSE Ti-E light microscope. All phase images were taken with 30 ms exposure time for consistency. To evaluate the fabrication resolution, extra chips composed of pillars with diameters ranging from 500 μm to 1000 μm with 100 μm increment were fabricated. 5 diameter measurements for posts of different sizes were conducted using the open software ImageJ (NIH,

USA), based on which the standard deviation δ_r is calculated. A tabletop scanning electron microscope (SEM) (Hitachi, TM3000) was also used to characterize the solid structure [for the photo shown in Fig. 1(A)].

Surface modification

The wetting properties of PDMS-based solids can be altered *via* oxygen plasma treatment.[43] This approach is adopted as the surface modification method to generate temporarily hydrophilic PDMS-based solid structures. Specifically, the treatment is applied at medium radio frequency (RF) at 38 W for 60 seconds using the PDC-002-HP Harrick Plasma Cleaner. After treatment, the contact angle is characterized using the sessile drop method, where the image was captured using a 5MP digital USB microscope, and the contact angle was measured *via* the built-in angle measurement tool in ImageJ. Please refer to Fig. S1(A)† for the contact angles as a function of elapsed time after oxygen plasma treatment. We note that it is possible to further tune the contact angle alteration by changing the treatment conditions, such as RF intensity as well as treatment length.

Fluid flow experiment

Following the surface wettability modification, the experiments with hydrophilic solid structures were conducted right after the plasma treatment, whereas we waited for at least 3 days before conducting experiments for hydrophobic solid structures.

The inlet and outlets of the capped devices were fitted with 1/64″ ID Tygon tubing (Cole Parmer, USA). The tubings were fitted to Luer adaptors (Cole Parmer, USA) before connecting to 1-way stopcocks. Fluid flow into the devices was established using a syringe pump (LEGATO 111) with a 1 mL syringe connected to the inlet's stopcock. Perfusion rate was kept constant at 0.16 μL min^{-1} and 2 μL min^{-1} for hydrophilic and hydrophobic devices, respectively. The fluid invasion processes within the devices were recorded using a 5MP digital USB microscope, and the *in situ* contact angles in poroFluidic devices were measured from the captured movies [Fig. S1(B)†]. These measured contact angles (mean and standard deviation) were used in corresponding numerical simulations.

For experiments with conductive carbon paint–water mixtures shown in Fig. 3(F), the conductive paint (Bare Conductive, UK) was thoroughly mixed with water with volume ratios 1 : 10 and 1 : 1. The dynamics viscosities were measured to be 7.4 mPa s and 46.9 mPa s, respectively, using the Anton Paar Dynamic Sheer Rheometer (SmartPave 92, Anton Paar, Austria). Injection rates of 0.1 μL min^{-1} and 0.02 μL min^{-1} were imposed at the inlet for the 1 : 10 and 1 : 1 volume ratio fluids, respectively.

Numerical method

The pore-resolved interface tracking algorithm was used for all multi-phase flow simulations.[24] Please see ESI† (ESI Text and Fig. S2) for further details about the numerical method.

Data availability

The authors confirm that the data supporting the findings of this study are available within the article and its ESI† materials.

Author contributions

Z. W., Y. G., and J.-M. P conceived the research. L. J. Y. O. and Z. W. conducted the experiments, Z. W. conducted the simulations. Z. W. and L. J. Y. O. analyzed the results. Z. W., L. J. Y. O., Y.-C. T. and E. S. wrote and edited the manuscript. All authors reviewed the manuscript.

Conflicts of interest

The authors declare no competing interests.

Acknowledgements

References

1 H. Stone, A. Stroock and A. Ajdari, *Annu. Rev. Fluid Mech.*, 2004, **36**, 381–411.

2 S. Battat, D. A. Weitz and G. M. Whitesides, *Lab Chip*, 2022, **22**, 530–536.

3 H. Ragelle, M. W. Tibbitt, S.-Y. Wu, M. A. Castillo, G. Z. Cheng, S. P. Gangadharan, D. G. Anderson, M. J. Cima and R. Langer, *Nat. Commun.*, 2018, **9**, 1184.

4 I. R. Woodward, L. Attia, P. Patel and C. A. Fromen, *AIChE J.*, 2021, **67**, e17452.

5 I. R. Woodward and C. A. Fromen, *Addit. Manuf.*, 2021, **48**, 102386.

6 F. Kotz, P. Risch, K. Arnold, S. Sevim, J. Puigmartí-Luis, A. Quick, M. Thiel, A. Hrynevich, P. D. Dalton, D. Helmer and B. E. Rapp, *Nat. Commun.*, 2019, **10**, 1439.

7 K. Dubil, T. Wetzel and B. Dietrich, *Int. J. Heat Mass Transfer*, 2023, **200**, 123546.

8 X. Zheng, W. Smith, J. Jackson, B. Moran, H. Cui, D. Chen, J. Ye, N. Fang, N. Rodriguez, T. Weisgraber and C. M. Spadaccini, *Nat. Mater.*, 2016, **15**, 1100–1106.

9 N. A. Dudukovic, E. J. Fong, H. B. Gemeda, J. R. DeOtte, M. R. Cerón, B. D. Moran, J. T. Davis, S. E. Baker and E. B. Duoss, *Nature*, 2021, **595**, 58–65.

10 K. D. Fink, J. A. Kolodziejska, A. J. Jacobsen and C. S. Roper, *AIChE J.*, 2011, **57**, 2636–2646.

11 J. Esarte, J. M. Blanco, A. Bernardini and R. Sancibrián, *Appl. Sci.*, 2019, **9**, 2905.

12 C. Ferroni, F. S. Franchi, M. Ambrosetti, M. Bracconi, G. Groppi, M. Maestri and E. Tronconi, *ACS Eng. Au*, 2022, **2**, 118–133.

13 M. Blunt, F. F. John and F. M. Orr, *Energy Convers. Manage.*, 1993, **34**, 1197–1204.

14 L. W. Lake, R. Johns, B. Rossen and G. Pope, *Fundamentals of Enhanced Oil Recovery*, Society of Petroleum Engineers, 2014.

15 J. Lipiec, J. Kuś, A. Słowińska-Jurkiewicz and A. Nosalewicz, *Soil Tillage Res.*, 2006, **89**, 210–220.

16 M. L. Szulczewski, C. W. MacMinn, H. J. Herzog and R. Juanes, *Proc. Natl. Acad. Sci.*, 2012, **109**, 5185–5189.

17 M. J. Blunt and Q. Lin, *Engineering*, 2022, **14**, 10–14.

18 R. Lenormand, E. Touboul and C. Zarcone, *J. Fluid Mech.*, 1988, **189**, 165–187.

19 K. Singh, H. Scholl, M. Brinkmann, M. D. Michiel, M. Scheel, S. Herminghaus and R. Seemann, *Sci. Rep.*, 2017, **7**, 444.

20 F. Guo and S. A. Aryana, *Energies*, 2019, **12**, 1390.

21 B. Zhao, C. W. MacMinn and R. Juanes, *Proc. Natl. Acad. Sci.*, 2016, **113**, 10251–10256.

22 H. S. Rabbani, D. Or, Y. Liu, C.-Y. Lai, N. B. Lu, S. S. Datta, H. A. Stone and N. Shokri, *Proc. Natl. Acad. Sci.*, 2018, **115**, 4833–4838.

23 Q. Gu, H. Liu and L. Wu, *J. Fluid Mech.*, 2021, **915**, A138.

24 Z. Wang, J.-M. Pereira, E. Sauret, S. A. Aryana, Z. Shi and Y. Gan, *Adv. Water Resour.*, 2022, **162**, 104152.

25 M. Cieplak and M. O. Robbins, *Phys. Rev. Lett.*, 1988, **60**, 2042–2045.

26 M. Trojer, M. L. Szulczewski and R. Juanes, *Phys. Rev. Appl.*, 2015, **3**, 054008.

27 W. Lei, X. Lu, F. Liu and M. Wang, *J. Fluid Mech.*, 2022, **942**, R5.

28 R. Holtzman, *Sci. Rep.*, 2016, **6**, 36221.

29 Z. Wang, K. Chauhan, J.-M. Pereira and Y. Gan, *Phys. Rev. Fluids*, 2019, **4**, 034305.

30 R. Hu, T. Lan, G.-J. Wei and Y.-F. Chen, *J. Fluid Mech.*, 2019, **875**, 448–475.

31 N. B. Lu, C. A. Browne, D. B. Amchin, J. K. Nunes and S. S. Datta, *Phys. Rev. Fluids*, 2019, **4**, 084303.

32 Z. Wang, J.-M. Pereira and Y. Gan, *Water Resour. Res.*, 2021, **57**, e2020WR029415.

33 W. Purcell, *J. Pet. Technol.*, 1950, **2**, 11–12.

34 M. Cieplak and M. O. Robbins, *Phys. Rev. B: Condens. Matter Mater. Phys.*, 1990, **41**, 11508–11521.

35 R. Holtzman and E. Segre, *Phys. Rev. Lett.*, 2015, **115**, 164501.

36 Z. Wang, J.-M. Pereira, E. Sauret and Y. Gan, *J. Fluid Mech.*, 2022, **941**, A40.

37 B. K. Primkulov, S. Talman, K. Khaleghi, A. Rangriz Shokri, R. Chalaturnyk, B. Zhao, C. W. MacMinn and R. Juanes, *Phys. Rev. Fluids*, 2018, **3**, 104001.

38 R. Lenormand, *J. Phys.: Condens. Matter*, 1990, **2**, SA79–SA88.

39 P. Concus and R. Finn, *Proc. Natl. Acad. Sci.*, 1969, **63**, 292–299.

40 S. Golmohammadi, Y. Ding, M. Küchler, D. Reuter, S. Schlüter, M. Amro and H. Geistlinger, *Water Resour. Res.*, 2021, **57**, e2021WR029908.

41 B. Venzac, S. Deng, Z. Mahmoud, A. Lenferink, A. Costa, F. Bray, C. Otto, C. Rolando and S. Le Gac, *Anal. Chem.*, 2021, **93**, 7180–7187.

42 L. J. Y. Ong, T. Ching, L. H. Chong, S. Arora, H. Li, M. Hashimoto, R. DasGupta, P. K. Yuen and Y.-C. Toh, *Lab Chip*, 2019, **19**, 2178–2191.

43 M. Morra, E. Occhiello, R. Marola, F. Garbassi, P. Humphrey and D. Johnson, *J. Colloid Interface Sci.*, 1990, **137**, 11–24.